

Full length article

Quantitative 3D structural analysis of the cellular microstructure of sea urchin spines (II): Large-volume structural analysis

Hongshun Chen^a, Ting Yang^a, Ziling Wu^b, Zhifei Deng^a, Yunhui Zhu^b, Ling Li^{a,*}

^a Department of Mechanical Engineering, Virginia Tech, Blacksburg, VA 24060, USA

^b Department of Electrical and Computer Engineering, Virginia Tech, Blacksburg, VA 24060, USA

ARTICLE INFO

Article history:

Received 14 November 2019
Revised 3 March 2020
Accepted 3 March 2020
Available online 7 March 2020

Keywords:

Sea urchin spines
X-ray computed tomography
3D network topology
Cellular solids
Mechanical property

ABSTRACT

Biological cellular materials have been a valuable source of inspiration for the design of lightweight engineering structures. In this process, a quantitative understanding of the biological cellular materials from the individual branch and node level to the global network level in 3D is required. Here we adopt a multiscale cellular network analysis workflow demonstrated in the first paper of this work series to analyze the biomineralized porous structure of sea urchin spines from the species *Heterocentrotus mamillatus* over a large volume (ca. 0.32mm³). A comprehensive set of structural descriptors is utilized to quantitatively delineate the long-range microstructural variation from the spine center to the edge region. Our analysis shows that the branches gradually elongate (~50% increase) and thicken (~100% increase) from the spine center to edge, which dictates the spatial variation of relative density (from ~12% to ~40%). The branch morphology and network organization patterns also vary gradually with their positions and orientations. Additionally, the analysis of the cellular network of individual septa provides the interconnection characteristics between adjacent septa, which are the primary structural motifs used for the construction of the cellular structure in the edge region. Lastly, combining the extracted long-range cellular network and finite element simulations allows us to efficiently examine the spatial and orientational dependence of local effective Young's modulus across the spine's radius. The structural-mechanical analysis here sheds light on the structural designs of *H. mamillatus*' porous spines, which could provide important insights for the design and modeling of lightweight yet strong and damage-tolerant cellular materials.

Statement of Significance

Previous investigations on the cellular structures of sea urchin spines have been mainly based on 2D measurements or 3D quantification of small volumes with limited structural parameters. This limits our understanding of the interplay between the 3D microstructural variations and the mechanical properties in sea urchin spines, which hence constrains the derivation of the underlying principles for bio-inspired designs. This work utilizes our multiscale 3D network analysis, for the first time, to quantify the 3D cellular network and its variation across large volumes in sea urchin spines from individual branch and node level to the cellular network level. The network analysis demonstrated here is expected to be of great interest to the fields of biomineralization, functional biological materials, and bio-inspired material design.

Published by Elsevier Ltd on behalf of Acta Materialia Inc.

1. Introduction

Many organisms construct their structural skeletons based on porous microstructures, such as wood [1–3], trabecular bone [4–6], and echinoderms' skeletal elements (e.g., ossicles in starfish, spines

and tests in sea urchins) [7,8]. These materials usually possess unique combinations of structural and mechanical properties such as low density, controlled anisotropy, high strength and damage tolerance via their judicious control over the spatial distribution of solid materials across multiple length scales. In particular, the biomineralized skeletal elements in echinoderms, which are composed of highly porous magnesium calcite meshwork (mineral content > 99 wt%) [9], known as stereom, represent a unique group of natural cellular materials because of their characteristic

* Corresponding author.

E-mail address: lingl@vt.edu (L. Li).

morphology and mechanical properties [10–12]. The echinoderms' stereom structures show vast variations among different species, within different skeletal elements in an individual animal, and even within the same skeletal element [13–15]. Quantitative description and understanding of the 3D porous structure from the individual branch (or trabecula) and node (or interconnection) level to the global network level is required for further understanding of the mechanical design and morphogenesis mechanisms of these cellular structures as well as for the development of biomimicry analogs. In the first paper of this work series, we reported a multiscale cellular network analysis pipeline tailored for echinoderms' stereom structures. In this second paper, we utilize this methodology to conduct a systematic analysis of the stereom structure from the sea urchin spines from *Heterocentrotus mamillatus* (Linnaeus, 1758) over a large volume.

The sea urchin *H. mamillatus* has been a popular model system for studying the structural designs and mechanical properties of sea urchin spines, which is mainly motivated by its remarkable damage tolerance through the “graceful failure” behavior [9,11,16–19]. This lightweight material also achieves excellent penetration resistance under local indentation loading [11,20,21]. The multiscale structures of *H. mamillatus* spines, similar to other echinoderms' stereoms, have been elucidated by numerous studies through 2D imaging analysis primarily based on scanning electron microscopy (SEM) [13–15,18,22]. Following Smith's classification on stereom's structural types [10,13], the stereom structures in *H. mamillatus*' spines have been qualitatively described as the laminar stereom with a multilayered construction in the center region (also known as medulla), and the labyrinthic stereom with radial alignment (known as septa) between center and growth rings, which are the micro-perforate stereom with a much lower porosity [9–11,16]. The *H. mamillatus* spines thus represent one of the most delicately designed stereom structures among all sea urchin species. Based on 2D SEM images, the organization of branches and pores has been described by several parameters such as pore diameter and branch size, suggesting a certain degree of orderliness in the stereom of different regions [14,23].

Previous 2D-based investigations on *H. mamillatus*' stereom structures are inadequate to provide quantitative information of their 3D morphology of individual branches and nodes as well as the porous network organization at the skeletal level. Recent 3D analysis based on X-ray micro-computed tomography (μ -CT) provides qualitative visualization and characterization of internal 3D microstructures (e.g., smooth transition between branches, branch profile, etc.) of echinoderms' stereoms [24–27]; however, the quantitative analysis in 3D has often been limited to porosity estimation or small volume analysis [12,15]. Here we conduct a quantitative cellular network analysis of the *H. mamillatus*' spines at skeletal level via the methodology presented in the first paper of this work series. Compared to previous investigations, a more comprehensive set of structural descriptors was adopted to elucidate both short- and long-range structural characteristics in 3D of the *H. mamillatus* spines (Fig. S1 and Table 1), including (i) node characteristics; (ii) inter-branch angle; (iii) curved branch length and node-to-node branch length (i.e., branch distance); (iv) tortuosity; (v) average, minimum, and central branch thicknesses; (vi) branch morphology; (vii) branch orientation; and (viii) ring structure. The correlations between branch location and parameters (i) and (iii)–(v), as well as the correlations between branch orientation and structural parameters (i) and (iii)–(v) were investigated. Moreover, structural analysis was performed on isolated septa to investigate the interconnection characteristics between adjacent septa. The cellular network information obtained from this multiscale analysis is also used to investigate the spatial variation of the mechanical properties across the entire volume of interest via finite element modeling of the extracted cellular networks.

Table 1
Illustration of each descriptor for structural analysis.

| Descriptor name | Explanation |
|---------------------|---|
| Nodal configuration | The connectivity (or coordination number) of each node, N- i type with $i = 3$ –6 denoting the coordination number; |
| N-3 orientation | 3D orientation of the normal of the plane formed by a N-3 node; |
| Branch length | The length of the curved path between two nodes (l); |
| Branch distance | The Euclidean distance between two nodes (d); |
| Tortuosity | The ratio of branch length to branch distance (l/d); |
| Inter-branch angle | The angle between two branches at each N-3 or N-4 node (γ); |
| Branch thickness | The average (\bar{t}), minimum (t_{\min}), and central thicknesses (t_{cen}) or the thickness at different location of a branch (t_i); |
| Branch morphology | The profile of the branch surface which is quantitatively described by an even 4-th order polynomial; |
| Branch orientation | The orientation of branch about principal axes of the spine, θ denotes the angle between a branch and L direction, ω denotes the angle between projected branch onto the R-C plane and the R direction; |
| Ring structure | Loop formed by a certain number of successively connecting nodes, i-B type with $i = 4$ –7 denoting the number of connected branches forming the ring; |
| Ring size | The diameter of the fitted circle in the fitted ring plane (d_{ring}). |

* θ , ω , l , d , \bar{t} , t_{\min} , t_{cen} , and t_i are defined in Fig. S1.

2. Materials and methods

2.1. Specimens and electron microscopy

Dried *H. mamillatus* spine specimens were purchased from Etsy Inc. The cylindrical shape of the spines measures 1.0–1.5 cm in diameter and ca. 10 cm in length (Fig. 1A and B). A cylindrical coordinate system is used throughout this work, where L, R, and C represent the spines' longitudinal, radial, and circumferential directions, respectively. SEM images were obtained from FEI Quanta 600 FEG with a typical working distance of 8 mm and an acceleration voltage of 5 kV. Samples were coated with platinum/palladium (~15 nm) prior to SEM imaging.

2.2. Synchrotron-based μ -CT measurement

The synchrotron-based μ -CT measurement was conducted at the beamline 2-BM at the Advanced Photon Source (APS), Argonne National Laboratory. A monochromatic beam (centered at 27.4 keV, corresponding to a wavelength of 0.45 Å) was used. 1500 projection images were acquired over a 180-degree rotation for each tomography scan with a rotation speed of 0.5°/s. The projection images were collected by using a PCO Edge high speed CMOS detector (2560 × 1300 pixels). The imaging system was equipped with 5 × and 10 × long-working-distance objective lenses, resulting in an isotropic voxel size of 1.3 μ m and 0.65 μ m, with corresponding fields of view of 3.33 × 1.69 mm and 1.66 × 1.38 mm, respectively. For the data presented in this work, the 5 × objective lens was used in order to cover large scan volumes. The specimens were elongated blocks (~2 mm, ~2 mm, ~10 mm in L, C, and R directions, respectively) cut along the radial direction from the spine center to the periphery with a low-speed diamond saw (colored box, Fig. 1B). Consecutive scans along the R direction with ~90 μ m overlaps between adjacent scans were acquired. The tomography data were then stitched together using Fiji/ImageJ [28] to obtain single continuous 3D dataset for the entire rectangular block. Multiple specimens were scanned but the data analysis presented in this work is based on a single dataset.

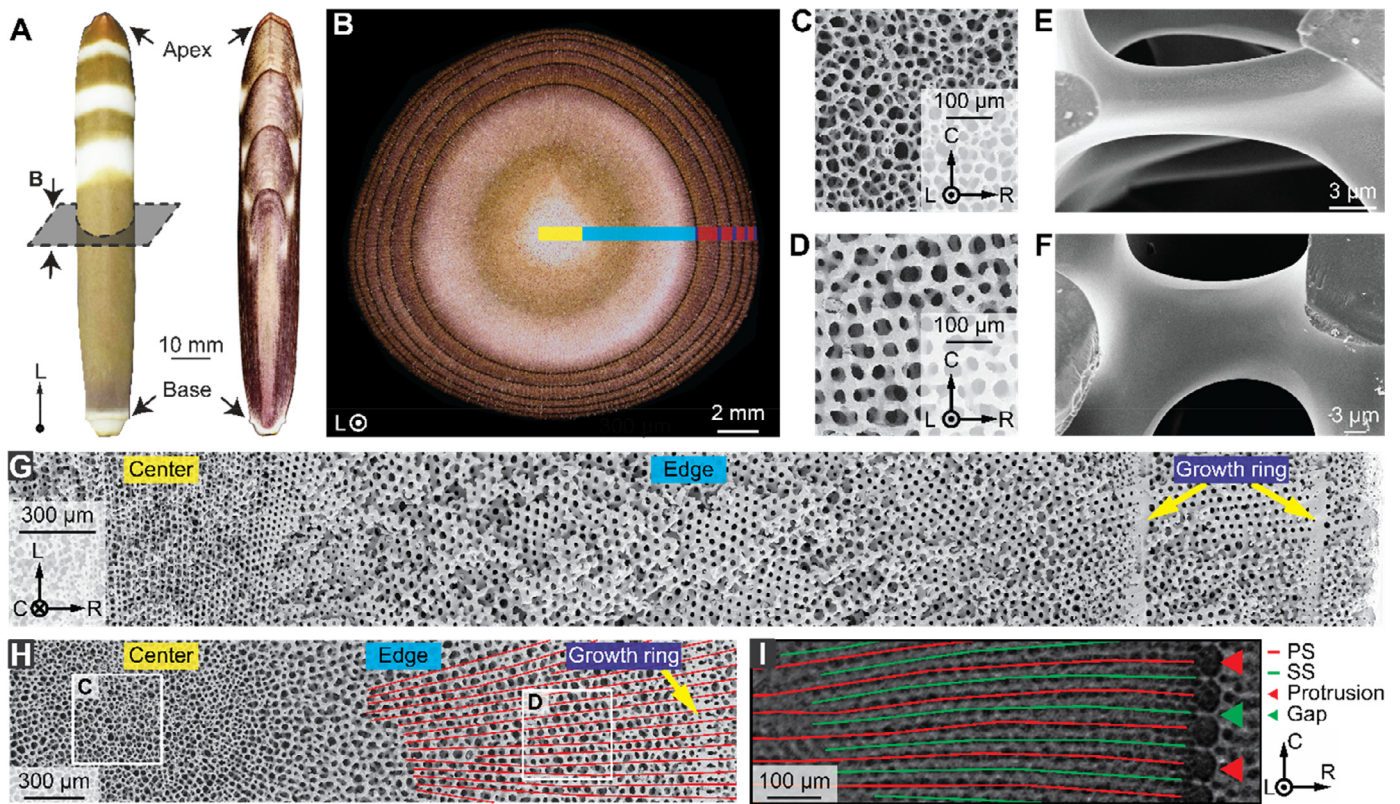


Fig. 1. An overview of the spine structure of *H. mamillatus*. (A) Optical image of the spine of *H. mamillatus* (left) and its cross-section cut along the longitudinal (L) direction (right). (B) Optical image of the transversely-cut cross-section of the spine (yellow area: center region; cyan area: edge region; red area: inter-growth ring stereom; blue area: growth ring). Scanning electron micrographs (SEM) images of the porous stereom in (C) the center region and in (D) the edge region with radiating septa as indicated in the white boxes in (H), respectively. SEM images of the representative branches (E) in the center region and (F) in the region of radiating stereom, respectively. SEM images of the cross-section of (G) L(longitudinal)-R(radial) plane and (H) R(radial)-C(circumferential) plane from the center region (left) towards the margin of the spine (right). Note that the growth rings are indicated by yellow arrows, and septa are traced by red lines. (I) Traces and definitions of primary septa (PS) and secondary septa (SS) based on X-ray projection images in the R-C plane. (For interpretation of the references to color in this figure legend, the reader is referred to the web version of this article.)

2.3. Multiscale cellular network analysis

The collected projection images were first reconstructed by using the open-source software TomoPy [29], which utilizes a standard Fourier grid reconstruction algorithm, one of the back-projection methods [30]. The reconstructed data was subsequently segmented by using another open-source, machine learning-based software ilastik [31]. We first trained the segmentation program by manually labeling some regions of the mineral phase in sea urchin spines. Then, the image stack was automatically labeled by Gaussian filters and Random Forest with 100 trees classifier [32]. The final stitched data and corresponding 3D rendering of the reconstructed and segmented volumes for analysis are shown in Fig. 2.

Next, we utilized the analysis pipeline developed in the first paper of this work series to conduct the quantitative characterization of the cellular network from the spine center to the edge [33]. This pipeline includes skeletonization, network cleaning and registration, and multiscale feature extraction and analysis [33]. In particular, the network cleaning step based on iterative branch trimming and node merging is necessary to eliminate dangling branches and node clusters, which is a significant issue for stereom-like structures with short and thick branches (see [33] for further details). Herein 5.9 μm and 6.5 μm were used as the merging distances for the center (sub-volumes 1–3, shaded in yellow) and edge (sub-volumes 4–10, shaded in cyan, Fig. 2A, D, and E) regions, respectively, in the skeleton trimming step. For the analysis here, we removed the branches and nodes within 19.5 μm from the periphery of the analyzed volume to avoid edge effects such as incomplete

branches. More detailed information about the methodology can be found in the first paper [33].

For the multiscale feature analysis based on the extracted cellular network, we utilized the same set of structural descriptors used in the first paper [33]. The brief explanation for each descriptor is given in Table 1 and the corresponding graphical representation is shown in Fig. S1. The detailed definitions can be found in the first paper of this work series [33]. In particular, to better account for the large branch morphology variation from the spine center to the edge region, instead of using the second-order polynomial to fit the extracted thickness profile of individual branches for a local region in the first paper [33], an even fourth-order polynomial was used here:

$$t_i(x_i)/t_{\min} = (a((x_i - x_{\min})/l)^2 + 1)^2, \quad (1)$$

where x_i is the coordinate of the location i measured from one end of the branch; t_i is the thickness at location i ; t_{\min} is the minimum thickness of the branch; x_{\min} is the coordinate at t_{\min} ; l is the branch length; and a is the fitting parameter (Fig. S1). Similar profiling functions with an even fourth-order polynomial has also been used for fitting branch thickness of synthetic open-cell foams [34–36]. Another modification is related to the ring detection algorithm introduced in first paper of this study [33]. The ring type is specified by the number of branches in a ring, such as 4-B, 5-B, 6-B, and 7-B rings. The centroids of the rings were calculated and considered as the locations of the rings. Here we carried out a plane fitting for the detected rings to evaluate the flatness of rings, where the method of linear least squares was used to calculate the

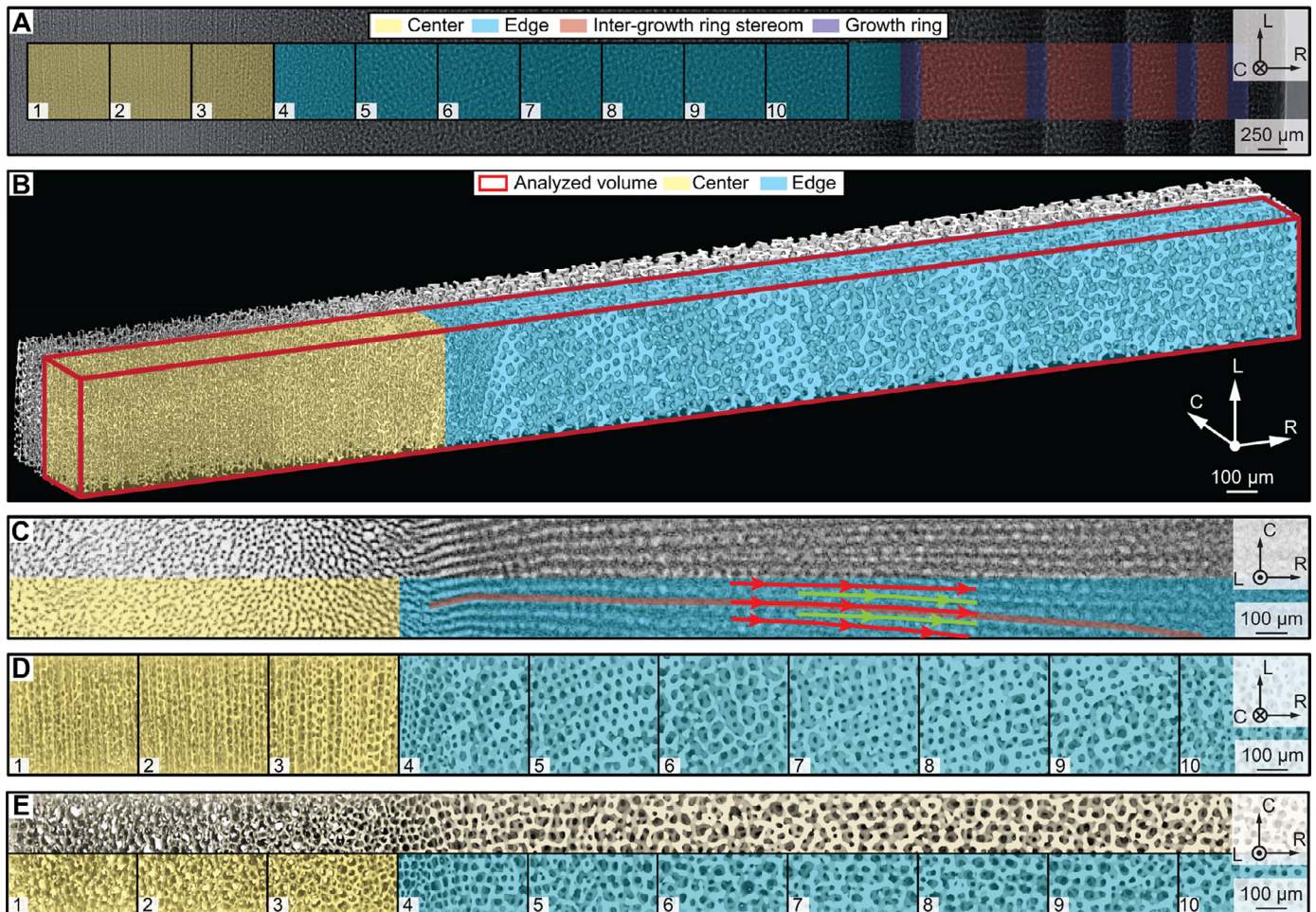


Fig. 2. Overview of the selected volume for structural analysis. (A) Synchrotron X-ray projection image of the imaged sample, which covers the volume from the spine center region to the margin of the spine: the center region (yellow boxes), the edge region (cyan boxes), the growth rings (blue boxes), and the inter-growth ring stereom (red boxes). The center and edge regions are separated in sub-volumes labeled by numbers 1 to 10 and used for quantitative analysis. The location and orientation of this sample is shown in Fig. 1B. (B) Volume rendering of the fully reconstructed stitched 3D volume with center and edge region differentiated (red box: the analyzed volume). (C) X-ray projection image of the analyzed volume in the R-C plane. The thick red line indicates a representative septum for analysis. The red and green streamlines represent the primary and secondary septa, respectively. Volume renderings of the (D) L-R and (E) R-C cross-section of the cut strip (area shaded with yellow and cyan: the center and edge regions, respectively, which were used for analysis). (For interpretation of the references to color in this figure legend, the reader is referred to the web version of this article.)

coefficient of determination (R^2) of the fitting. The fitting equation is as follow:

$$aX + bY + cZ + d = 0, \quad (2)$$

where a , b , c , and d , are coefficients of the 3D plane equation, X , Y , and Z denote the coordinates of the points on the branch in L, C, and R direction. We rearranged Eq. (2) into $F = -\frac{a}{c}X - \frac{b}{c}Y - \frac{d}{c}$, where F is the fitted value of Z . The following equation shows the calculation of R^2 .

$$R^2 = 1 - \frac{SS_{res}}{SS_{tot}}, \quad (3)$$

where $SS_{res} = \sum_i (F_i - \bar{Z})^2$ is the explained sum of squares, $SS_{tot} = \sum_i (Z_i - \bar{Z})^2$ is the total sum of squares. F_i represents the i th fitted value of the Z , Z_i is the i th data of the actual Z coordinate and \bar{Z} is the average value of all actual Z coordinate. The detected rings with $R^2 \geq 0.5$ (i.e., relatively flat rings) were selected for analysis here. Furthermore, the rings with a higher number of branches (higher-B rings) were neglected if there are lower-B rings with all nodes overlapped with the nodes of the corresponding higher-B rings, i.e., if the higher-B rings are composed of several lower-B rings.

2.4. Finite element analysis

The registered network connectivity and branch-level information allow us to construct beam models for static analysis. Abaqus/Standard 2016 (Dassault Systems, Vélizy-Villacoublay, France) was used to conduct mechanical Finite Element (FE) analysis. Ten representative volumes (each measures $195 \times 156 \times 195 \mu\text{m}$ in L, C and R directions, respectively) were isolated from the ten sub-volumes for finite element analysis. The models were meshed with the Timoshenko beam element B31 [37], and mesh size of $0.2 \mu\text{m}$ was used for all beam models. The average branch thickness of the corresponding branch obtained from the network analysis was assigned to each beam. The resulted number of branches and beam mesh for each model are listed in Table S1. The effective isotropic elastic modulus and the Poisson's ratio of calcite used in the simulations were 109 GPa and 0.291, respectively [38]. The model was subjected to compression by using two hypothetical rigid plates meshed with 2D discrete rigid elements (Fig. S2). The beam elements within $10 \mu\text{m}$ from the plates were tied to the plates. The compression simulation was achieved by fixing the bottom plate while the top plate was subject for loading in either L, C, or R direction with a maximum

strain of 0.1% (Fig. S2). Simulations along three principal directions (*i.e.*, the L, C, and R directions) for each sub-volume were conducted. The representative meshed model and the boundary conditions are shown in Fig. S2. The effective Young's modulus and stress contour were obtained from these compression simulations. Despite the potential discrepancy between the actual and simulated effective moduli due to the beam model used to represent thick and short beams in the edge region [39], our simulation results are sufficient for a comparative study to illustrate the trend of the spatial variations in effective modulus.

2.5. Statistical method

Descriptive statistics such as averages and standard deviations of the extracted structural descriptors as listed in Table 1 was used throughout the entire paper whenever possible. Violin plots (mirrored histograms) were used to evaluate the distribution of structural descriptors, where the number of data points corresponding to a given value range is indicated by the scale bar in each plot (*e.g.*, Figs. 4D and 5D). In addition, the standard deviations of the data were used as error bars.

3. Results

3.1. Structural overview of the analyzed volume

The *H. mamillatus* spines exhibit an intricate spatial control in their porous microstructure from the spine center to edge, as qualitatively summarized in Figs. 1 and 2. Here we broadly divided the cross section of the spine into the following four structural regions: (1) the center region, (2) the edge region with radiating septa, (3) the growth rings, and (4) the inter-growth ring stereom (Figs. 1B, G, H, and 2A). The center region is usually characterized by a lighter coloration shown in optical images (Fig. 1B). The stereom exhibits the Voronoi-like pattern of pores with thin branches of no preferred alignment when viewed in the R-C plane (Fig. 1C and D), consistent with the network analysis results conducted for a local volume in the center region [33]. In contrast, the edge region shows variations in pigmentation and the stereom has controlled radial alignment with much thicker branches (Fig. 1E and F). The growth rings are circular dense layering structures wrapping around the spines (Figs. 1B, G, I and 2A) [15,40]. According to previous studies, the number of growth rings in an individual spine varies from 1 to 12, depending on the age of sea urchins [40].

In this work, we focused our analysis on the volume from the center to the first growth ring, and the stereom beyond the first growth ring was not included, as shown in Fig. 2B and C. The reasons are two-fold. Firstly, as the stereom in the growth ring regions approaches to a fully dense structure, the current network analysis algorithm cannot accurately identify the underlying structure. Secondly, the stereom structures in the edge region and the inter-growth ring regions appear to have the same structural organization (Figs. 1G and 2A) [15]. The volume used for network analysis measures $0.390 \times 0.195 \times 4.193$ mm in the L, C, and R directions, respectively (Fig. 2B–E). The analyzed volume was divided into 10 sub-volumes for location-dependent structural and mechanical analysis, where sub-volumes 1–3 and 4–10 represent the center and edge regions, respectively (Fig. 2D and E). Fig. 2D and E show the 3D rendering of the volume of interest in L-R and R-C planes, respectively, from which the gradual change in branch morphology and size, as well as the network organization, can be observed.

The edge region is characterized by the radially aligned stereom, which is previously termed as the septum structure (Figs. 1H, I and 2C, E) [15]. Here, the μ -CT results reveal that the

septa can be further classified into two types, *i.e.*, the primary septa (PS) and secondary septa (SS) (Figs. 1I and 2C). The secondary septa represent the additional septa that are later inserted between two connecting adjacent primary septa when their spacing is increased to a threshold value of *ca.* 50 μ m. Based on the X-ray projection images in the R-C plane, the primary septa usually connect to the "solid protrusions" of the growth ring while the secondary septa extend to the gap between two adjacent primary septa (Fig. 1I). In the analyzed volume, sub-volume 7 marks the location of the initial insertion of one secondary septa, and sub-volume 4–6 and sub-volume 7–10 contain 4–5 and 2–3 primary septa, respectively (Fig. 2C–E). The branches connecting adjacent septa are denoted as interseptal branches (ISB).

3.2. Characteristics of nodes

Fig. 3 summarizes the node characteristics in the analyzed volume. Nodes with more than six connections (*i.e.*, N-7, N-8, *etc.*), comprising only 0.2% of all nodes ($N = 19,784$), were not considered in the analysis as they could be artifacts resulted from the node merging. The spatial distributions of N-3, N-4, N-5, and N-6 nodes are shown in Fig. 3A and B. Without seeing the clustering of a specific node type, we inferred a uniform spatial distribution of different node types. It can be concluded that for all sub-volumes, N-3 and N-4 nodes are the dominating node types in number, and the occasional appearance of N-5 and N-6 nodes may enhance the structural stiffness and strength [41]. The center region (*ca.* 150,000 nodes/mm³, sub-volume 1–3) has approximately twice the density of nodes as the edge region (*ca.* 60,000 nodes/mm³, sub-volume 4–10), with the maximum density of nodes in the sub-volume 3 towards the center/edge transition followed by a significant drop (sub-volume 4) (Fig. 3C). The ratios of N-3: N-4: N-5: N-6 nodes in each volume are, however, relatively conserved in ten sub-volumes (Fig. 3D).

We correlated the results of node characteristics with the X-ray projection images of the *H. mamillatus* spine where the primary septa, secondary septa, and interseptal branches can be clearly distinguished (Fig. S3). As expected, in the sub-volume 4 with no secondary septa, the nodes are predominantly located on the primary septa when viewed in the R-C plane. In contrast, the distribution of nodes is much more random and uniform in the sub-volume 7 due to the insertion of secondary septa.

We also performed analysis of the inter-branch angles for the N-3 and N-4 nodes of the entire volume (Fig. 3E and F). The mean and standard deviation for the smallest, median, and largest inter-branch angles for N-3 nodes are obtained as $95.90^\circ \pm 16.44^\circ$, $117.92^\circ \pm 10.96^\circ$, and $137.98^\circ \pm 13.15^\circ$, respectively ($N = 12,005$). The mean and standard deviation of all inter-branch angles of N-3 nodes is $117.27^\circ \pm 5.78^\circ$, which is close to the inter-branch angle of the ideal 3-branch node (*i.e.*, 120°). For N-4 nodes, the smallest and largest inter-branch angles are $84.13^\circ \pm 17.28^\circ$ and $133.17^\circ \pm 14.92^\circ$, respectively ($N = 6166$). The mean and standard deviation of all inter-branch angles of N-4 nodes is $108.69^\circ \pm 9.11^\circ$, which approaches to the bond angle of the idealized diamond lattice (*i.e.*, 109.5°).

A detailed analysis of the planarity index and orientation distribution for N-3 nodes was summarized in Fig. S4. The planarity index of an N-3 node is defined as the unitless distance between the node and the plane constructed by three unit vectors along the connecting branches starting from this node [33, 42]. The spatial distribution of the N-3 nodes colored by their corresponding planarity indices is presented in Fig. S4A and B, where location-dependent variation was not observed. 95% of the planarity indices is less than 0.3, which is within 18° offset from an ideal flat plane. The result agrees with the average inter-branch angle measurements of the N-3 nodes and demonstrates that the branches

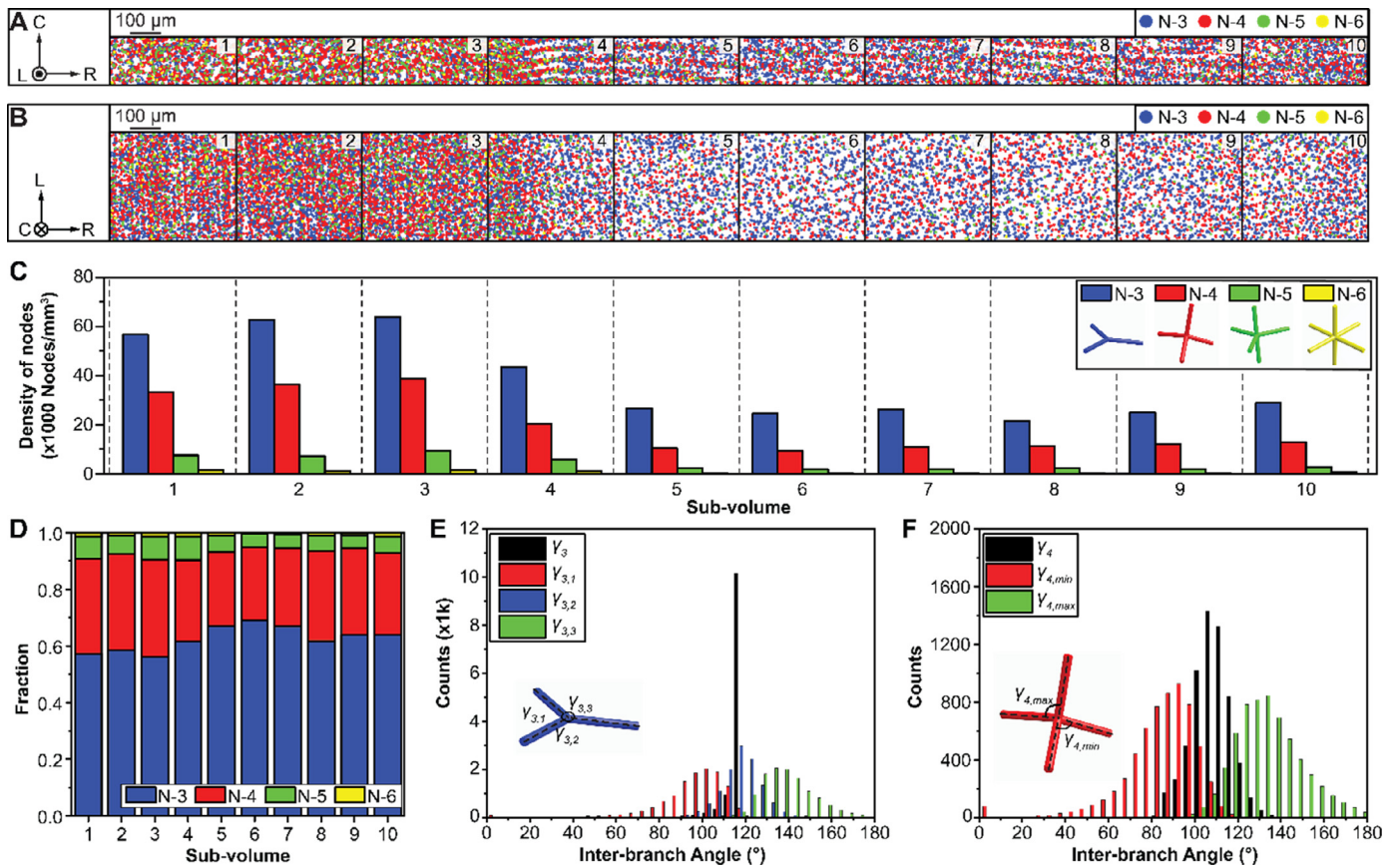


Fig. 3. Quantitative analysis of node characteristics in the volume of interest. Spatial distribution of nodes colored by node types visualized on (A) the R-C plane and (B) the L-R plane, respectively. Blue: N-3 nodes; red: N-4 nodes; green: N-5 nodes; yellow: N-6 nodes. The 10 sub-volumes are labeled numerically. (C) The density of different node types in ten separate sub-volumes. The inset shows the schematic diagrams of the ideal N-3, -4, -5 and -6 nodes. (D) Number fraction of different node types in ten separate sub-volumes. (E) Histogram of smallest ($\gamma_{3,1}$), median ($\gamma_{3,2}$), largest ($\gamma_{3,3}$) and mean ($\gamma_3 = (\gamma_{3,1} + \gamma_{3,2} + \gamma_{3,3})/3$) inter-branch angles for N-3 nodes. Inset: schematic diagram of the inter-branch angles for a N-3 node. (F) Histogram of the smallest ($\gamma_{4,min}$), largest ($\gamma_{4,max}$) and mean (γ_4) inter-branch angles for N-4 nodes. Inset: schematic diagram of the inter-branch angles for a N-4 node. (For interpretation of the references to colour in this figure legend, the reader is referred to the web version of this article.)

connecting to an N-3 node reside nearly in a common plane. The orientation distribution of the N-3 nodes with their corresponding planarity indices for each sub-volume is shown in Fig. S4C. For the orientation of N-3 nodes, θ and ω are defined as the angle between the normal of the plane formed by N-3 node (i.e., $\tilde{\nu}_{N-3}$, Fig. S1B) and L direction and the angle between the projection of $\tilde{\nu}_{N-3}$ on the R-C plane and the R direction, respectively (see details in Fig. S1B). A clear gradual transition is observed: in the center region (sub-volume 1–3), the N-3 nodes exhibit a preferred alignment with $\theta \approx 0^\circ$ or 90° , whereas the edge region exhibits no preferred distribution of θ angles; in contrast, the uniform distribution in ω is maintained throughout the entire volume (Fig. S4C). This result indicates that in the center region, the N-3 nodes preferably face along or perpendicular to the L direction, and for the N-3 nodes facing perpendicular to the L direction, they are randomly pointed in the R-C plane.

3.3. Characteristics of branches

As qualitatively demonstrated in Fig. 1D and F, the thickness (i.e., radius), length, and morphology of the branches vary significantly in different regions along the R direction. With the cellular network analysis, we quantified the variations on branch length and orientation (Fig. 4), branch distance (Fig. S5), tortuosity (Fig. S6), branch thickness (Figs. 5, S7, and S8) and branch morphology (Figs. 7 and S9) for the analyzed volume. A detailed analysis is also provided for the center/edge transition region (sub-volume 4)

and the region with the initial insertion of secondary septa (sub-volume 7) (Fig. 6).

3.3.1. Spatial distribution and alignment of branch

The spatial distribution of branches colored by their corresponding branch lengths in the entire volume is shown in Fig. 4A and B ($N = 32,573$). It is evident that the density of branches in the center (ca. 250,000 branches/mm³, sub-volume 1–3) is as more than twice as that in the edge region (ca. 100,000 branches/mm³, sub-volume 4–10) (Fig. 4A–D), which is the result of the high density of nodes in the center region (Fig. 3A–C). The orientation of branches exhibits a clear difference in the center and edge regions (Fig. 4C). More specifically, the angle θ as defined in Fig. S1 for the branches in the center (sub-volume 1–3) mostly approaches either to 0° or 90° , which indicates that most branches orient approximately parallel or perpendicular to the L direction (Fig. 4C). This result is consistent with the qualitative observation of preferred alignment of branches in the SEM image (Fig. 1G), 3D reconstruction (Fig. 2D), and the detailed analysis results performed in a small volume close to the center region in the first paper [33]. Such orderliness of branch orientations is not observed in the edge region (sub-volume 4–10, Fig. 4C).

3.3.2. Length, distance, and tortuosity of branch

Variation in the mean branch length (l) is observed in the sea urchin spine with a ~50% increase in the edge region (21–27 μm , sub-volume 4–10) as compared to the center region (18–19 μm ,

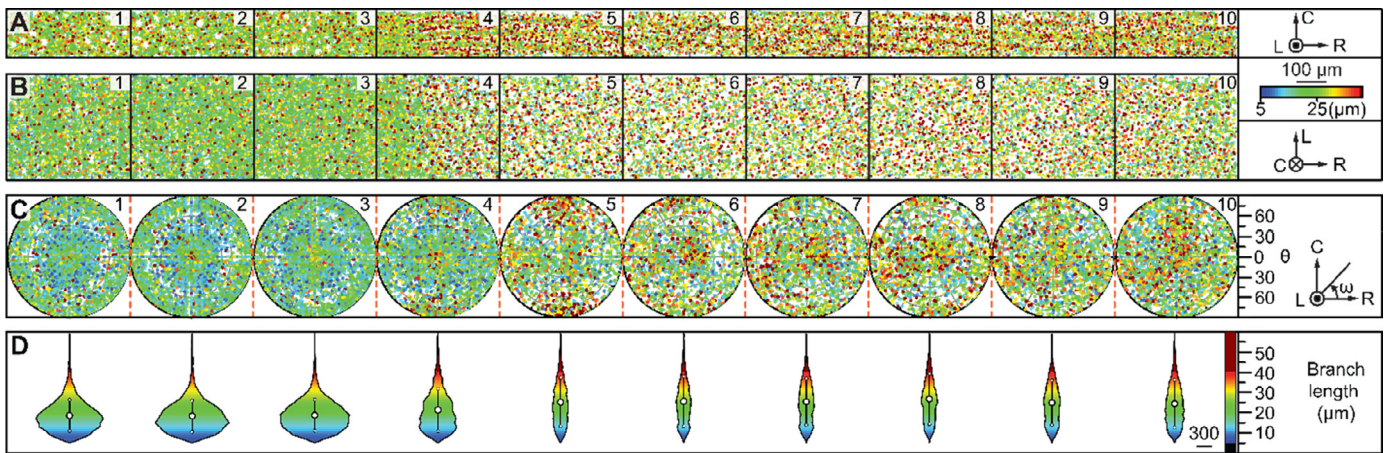


Fig. 4. Quantitative analysis of branch length. Spatial distribution of branches colored by branch length visualized on (A) the R-C plane and (B) the L-R plane, respectively. (C) The orientation of branches versus branch length of the ten separate sub-volumes. (D) Violin plots (mirrored histograms) of branch length for each sub-volume, where mean values and standard deviations are indicated as error bars. The number of data points corresponding to a given value range of the branch length is indicated by the scale bar on the lower right corner.

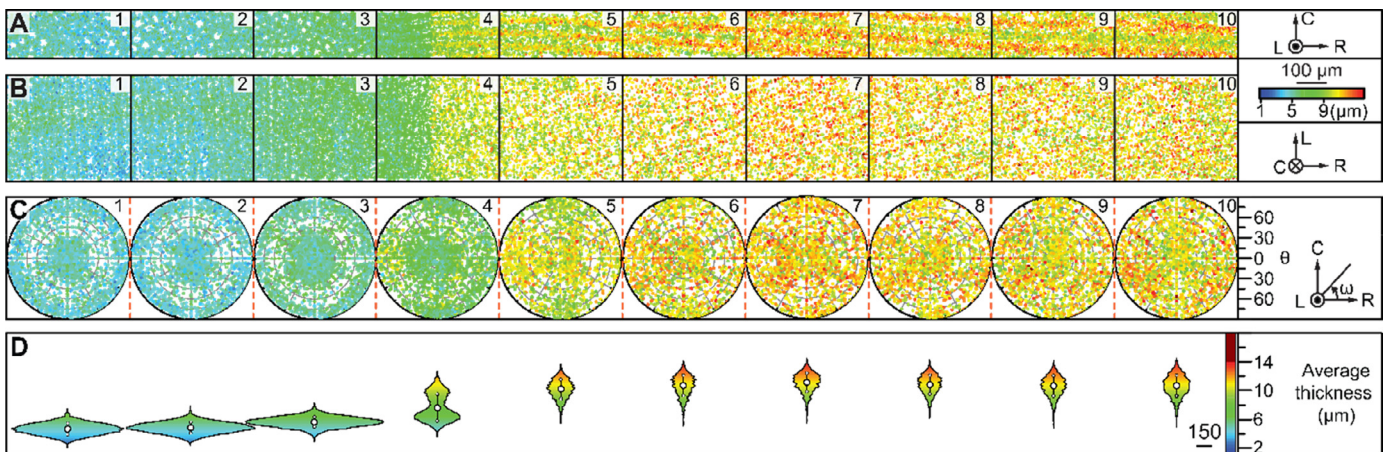


Fig. 5. Quantitative analysis of average branch thickness. Spatial distribution of branches colored by average thickness visualized on (A) the R-C plane and (B) the L-R plane, respectively. (C) The orientation of branches versus average thickness of the ten separate sub-volumes. (D) Violin plots (mirrored histograms) of average branch thickness for each sub-volume, where mean values and standard deviations are indicated as error bars. The number of data points corresponding to a given value range of the branch length is indicated by the scale bar on the lower right corner.

sub-volume 1–3) (Fig. 4D). Following the similar trend of l , the Euclidean distance between two connecting nodes (d) is ~50% higher in the edge region (18–22 μm, sub-volume 4–10) than in the center region (15–16 μm, sub-volume 1–3) (Fig. S5D). The tortuosity, defined as the ratio between branch length and branch distance (l/d), is therefore highly conserved throughout the entire volume and no spatial or orientational dependencies were observed (Fig. S6). 90% of the tortuosity values are smaller than 1.3, indicating that the majority of branches are only slightly curved.

We note that the branches on the primary septa are usually shorter than the interseptal branches connecting two adjacent primary septa (sub-volume 4), while the introduction of secondary septa in sub-volume 7 reduces this difference (Fig. 6A and B). This feature can be also observed in the branch length-orientation plots, where the yellow and red data points in the sub-volume 4 and 5 are concentrated to the branches with ω close to 90° and 270° and θ towards 90° (Fig. 4C).

3.3.3. Average, minimum, and central branch thickness

Figs. 5, S7, and S8 summarize the mapping of average, minimum, and central branch thickness, respectively, in relation to the branch location and orientation. Only branches with tortuosity less

than 2 and length within 5–40 μm were selected (98.6% of all branches) for branch thickness analysis to avoid artifacts (e.g., excessively long or curved branches) and inaccurate fitting of branch morphology. The following trends are observed:

- (i) The mean values of each measurement of thickness in the edge region (e.g., average thickness, 8–11 μm, sub-volume 4–10) are approximately twice as those in the center region (e.g., average thickness, 5–6 μm, sub-volume 1–3) (Figs. 5, S7, and S8), which is consistent with the previous 2D measurement in the similar positions of the spines [14].
- (ii) In the center region (sub-volume 1–3), the branches aligned closely along the L direction ($\theta < 30^\circ$) are slightly thicker (colored in cyan) compared to branches with $\theta > 60^\circ$ (see Figs. 5C, S7C, S8C and Table S2). This is also consistent with the results conducted on a small volume close to the center region in the first paper of this work series [33].
- (iii) In the edge region, the thickness exhibits a wider distribution than that in the center region (Figs. 5D, S7D, and S8D).
- (iv) According to the histograms shown in Figs. S7D and S8D, we found that the central thickness is on average ca. 0.5 μm thicker than the minimal thickness of a branch.

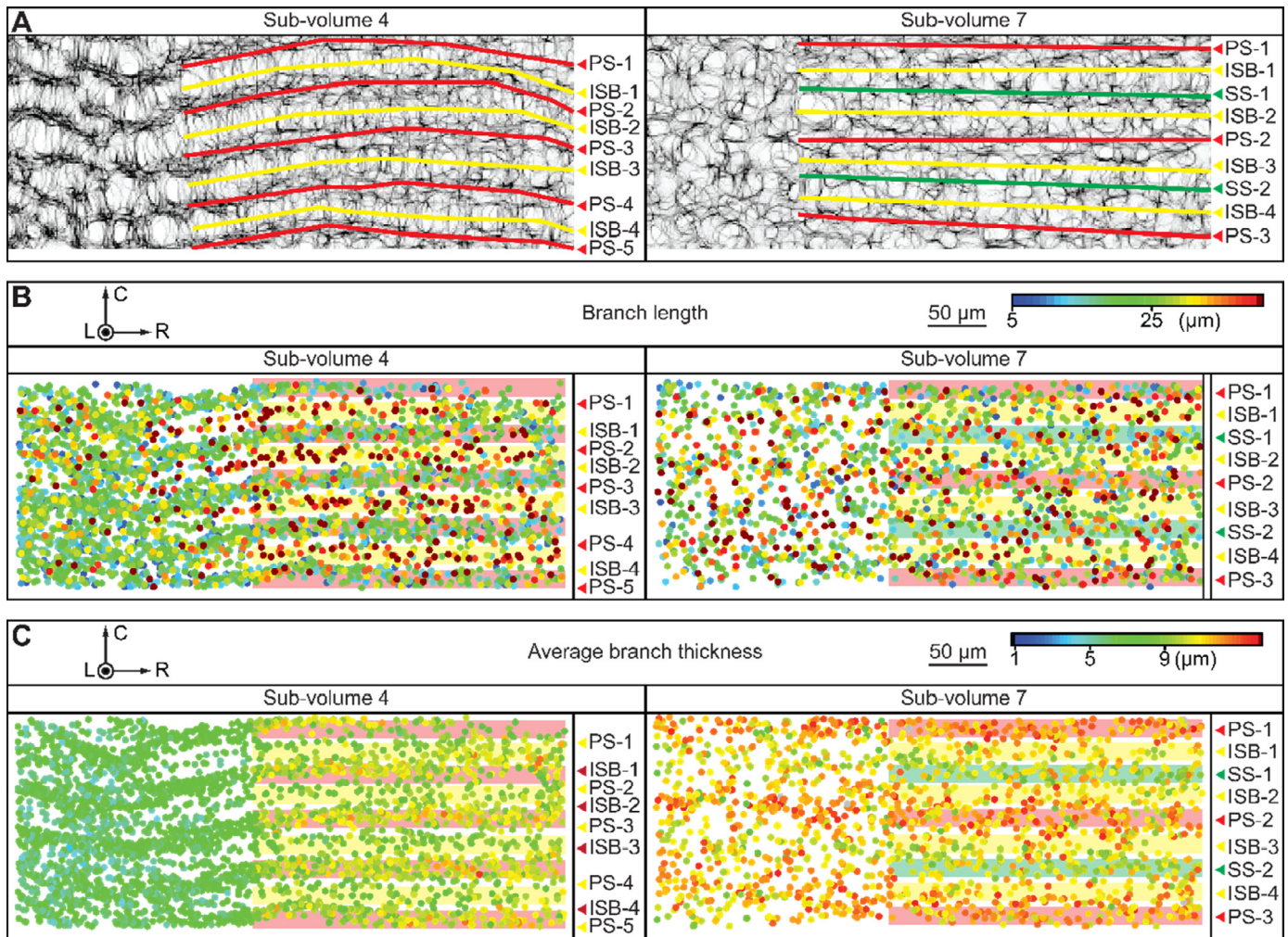


Fig. 6. Detailed structural analysis on the sub-volumes 4 and 7. (A) Trace of septa and interseptal branches based on the volumetric views on the R-C plane. (Red arrow & red line: primary septa; green arrow & green line: secondary septa; yellow arrow & yellow line: interseptal branch). Spatial distribution of branches colored by (B) branch length and (C) average branch thickness visualized on the R-C plane, respectively. The backgrounds in (B) and (C) are shaded by PS (red), SS (green), and ISB (yellow), respectively. (For interpretation of the references to color in this figure legend, the reader is referred to the web version of this article.)

- (v) The branches comprising the primary septa plane are thicker than the branches connecting adjacent septa (e.g., average branch thickness, 9.8 μm vs. 9.2 μm, sub-volume 4) and the branches on secondary septa (e.g., average branch thickness, 11.5 μm vs. 10.5 μm, sub-volume 7) (Fig. 6A and C. Also see the detailed quantification in Section 3.5).

3.3.4. Surface morphology of branch

The spatial and orientational distribution of the fitting parameter a used to describe the curviness of branches is summarized in Fig. 7A–C. The result indicates that the branches in the center region (yellow and red data points, sub-volume 1–3) are steeper (i.e., larger a 's) than those in the edge region (blue and cyan data points, sub-volume 4–10) (Fig. 7A–C). The variation of branch morphologies in each sub-volume can be better visualized in Fig. 7D, where all thickness data in each sub-volume were fitted together using Eq. (1). The mean of the minimum thickness and mean branch length in each sub-volume were used as t_{\min} and l , respectively, in Eq. (1) to calculate the average thickness (t_i) at each location of a branch (x_i) in the corresponding sub-volume. It can be clearly observed that branches in the center region (sub-volume 1–3, Fig. 7D) have steeper curvature in surface morphologies, which is primarily due to the relatively short and thin branch in the center region (Figs. 4D and 5D). In addition, in the

center region, the branches with $\theta > 60^\circ$ usually have a curvier profile than the branches with $\theta < 30^\circ$, consistent with the SEM observations (Fig. S9).

3.4. Characteristics of ring structure

The distribution of detected ring structures for different ring types is shown in Fig. 8A and B. As a result of a relatively larger density of nodes and branches, more rings exist in the center region (ca. 280,000 rings/mm³, sub-volume 1–3) than in the edge region (ca. 120,000 rings/mm³, sub-volume 4–10) (Fig. 8D). In all sub-volumes, the density of 4-B, 5-B, and 6-B rings are in increasing order, while the density of 7-B rings decreases (Fig. 8D). This suggests that the density of rings with more than 7 branches may further decrease and 5-B and 6-B rings take the dominant roles in constructing the spine's stereom structure. The majority of 5-B and 6-B rings in the structure, indicating a large amount of pseudo-hexagonal pattern, is considered a result of the large number of N-3 and N-4 nodes (Fig. 3C). Besides, the fraction of 4-B rings in the center region (16%–22%, sub-volume 1–3) is higher than that in the edge region (9%–14%, sub-volume 4–10) (Fig. S10). In addition, we observed a corresponding increase in the number fraction of 7-B rings in sub-volume 7, which is attributed to the insertion of the secondary septa that may lead to the local network modifications.

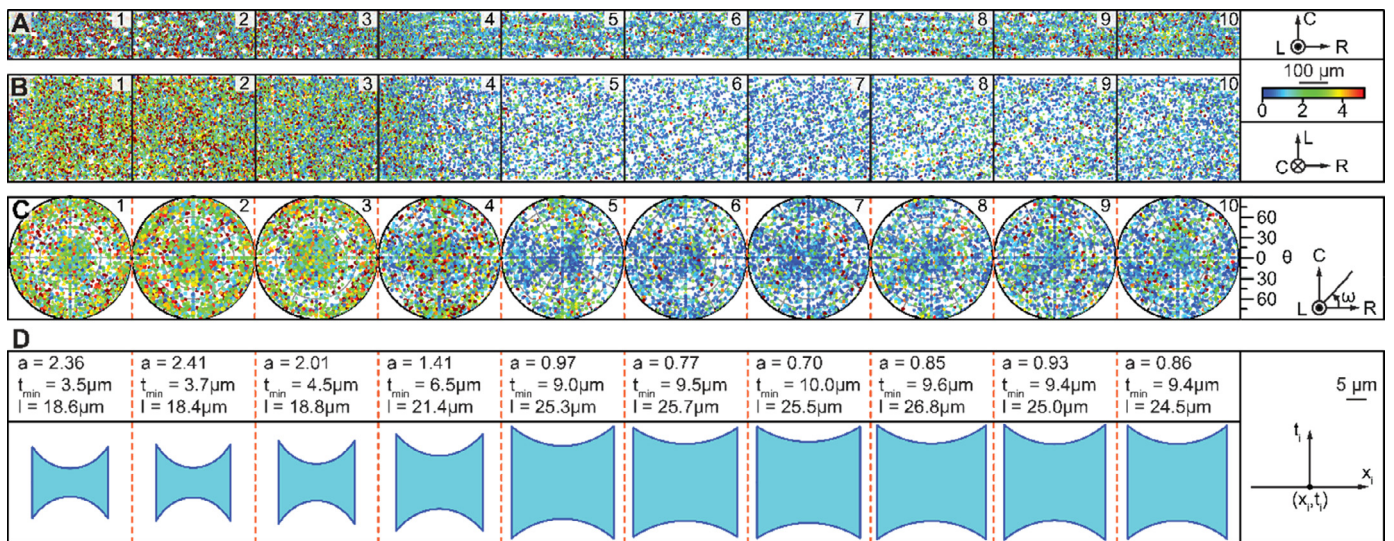


Fig. 7. Quantitative analysis of branch morphology. Spatial distribution of branches colored by their fitting parameters α as defined in Eq. (1) visualized on (A) the R-C plane and (B) the L-R plane, respectively. (C) The orientation of branches versus fitting parameters of ten separate sub-volumes. (D) Schematic diagrams of the branch morphology in ten separate sub-volumes along with the parameters substituted in Eq. (1).

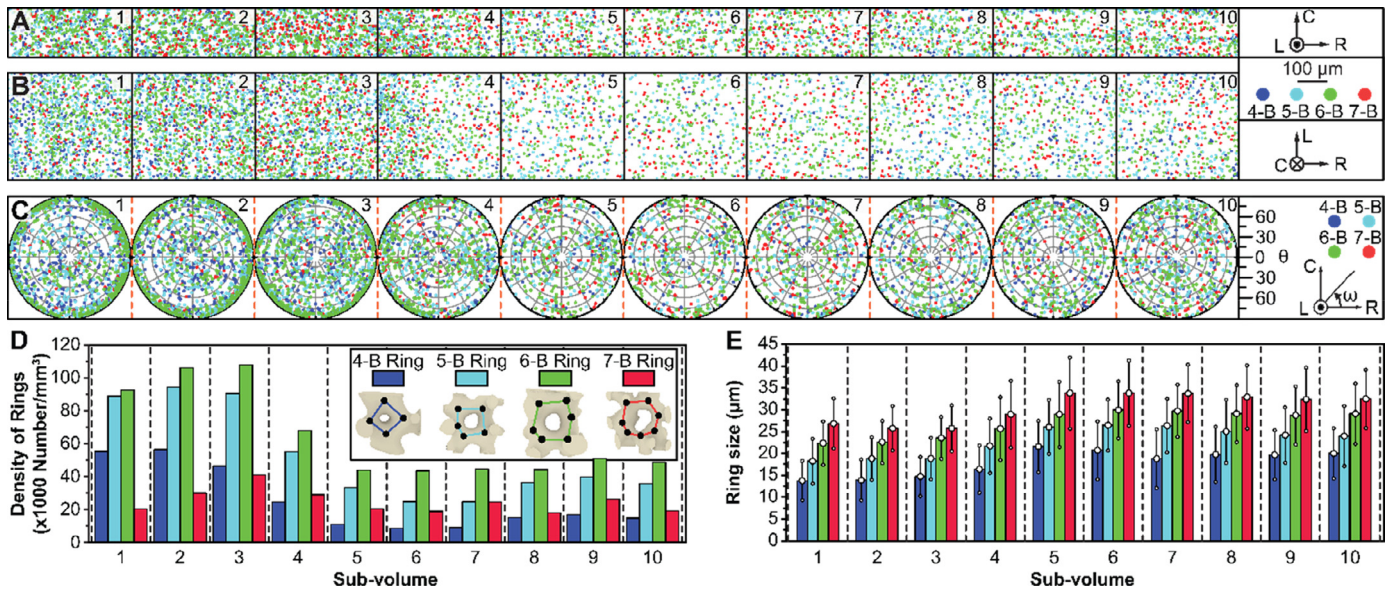


Fig. 8. Quantitative analysis of the ring structures. Spatial distribution of the identified rings colored by ring types visualized on (A) the R-C plane and (B) the L-R plane, respectively. Blue: 4-B rings; cyan: 5-B rings; green: 6-B rings; red: 7-B rings. (C) The orientation of rings versus ring types of ten separate sub-volumes. (D) The number density of different ring types in ten separate sub-volumes. Inset images show representative renderings of different ring types. (E) Histograms of the ring sizes for different ring types in ten separate sub-volumes.

The orientation of rings, described by the angle between the normal of the fitted ring plane and the L direction (θ) and the angle between the projected normal on the R-C plane and the R direction (ω), is correlated with different ring types as shown in Fig. 8C. Specifically, in the center region, a majority of the rings are oriented approximately perpendicular to the L direction ($\theta \approx 90^\circ$) without a dependency on ω , whereas this trend is less obvious in the edge region.

Following the first paper, the size of the rings (d_{ring}) is defined as the fitted diameter of the enclosed ring circle [33]. Despite the presence of variations, the mean ring sizes of 4-B, 5-B, 6-B, and 7-B are in increasing order (Fig. 8E). Each type of rings has approximately 1.4 times increase in size from the center to the edge region (Fig. 8E), consistent with the 2D measurements on pore sizes using

SEM images [14]. The ring size of each ring type is also correlated with the ring orientation as shown in Fig. S11A–D. Throughout the entire volume and for all types of rings, the rings with their normal directions pointing towards the R direction have a larger size (data points in green, yellow, and red) than those pointing to the C direction (data points in blue or cyan) (Fig. S11A–D). This is supported by the histogram of average size of rings of two separate orientations and of different types in each sub-volume (Fig. S11E), where the rings pointing towards the R direction ($-60^\circ \leq \omega \leq 60^\circ$ or $120^\circ \leq \omega \leq 240^\circ$) are ~ 1.3 times larger in diameter than those pointing towards the C direction ($60^\circ \leq \omega \leq 120^\circ$ or $240^\circ \leq \omega \leq 300^\circ$) (Table S3). The orientation-dependency of ring size (Fig. S11A–D) suggests that the branches comprising the septum is more closely packed than the branches connecting the adjacent septa.

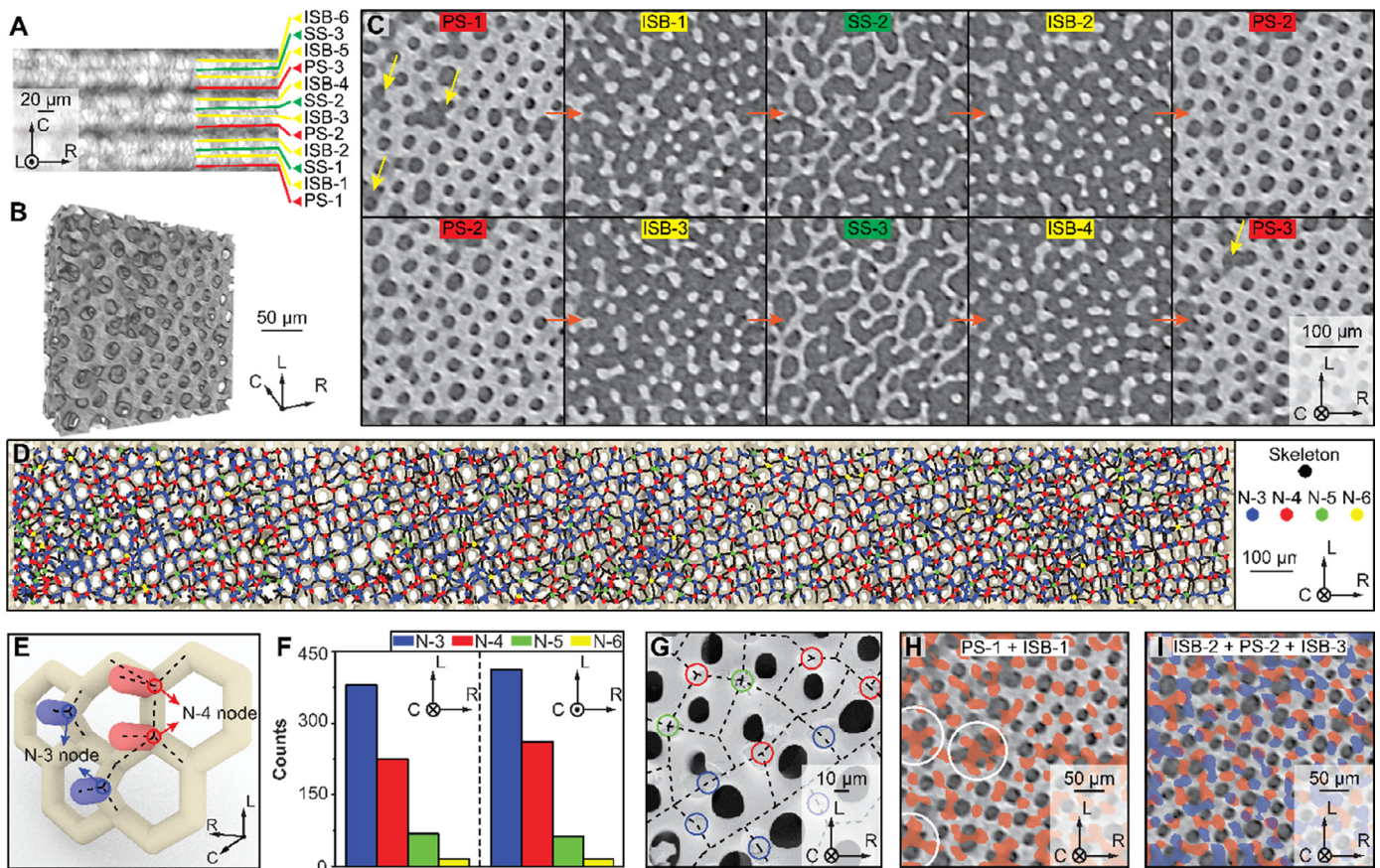


Fig. 9. Structural analysis of septa. (A) A representative X-ray projection image taken from the edge region, illustrating the presence of the primary septa (PS, red lines), secondary septa (SS, green lines), and interseptal branches (ISB, yellow lines) when viewed in the R-C plane. (B) A 3D rendering of the corresponding volume. (C) A sequence of reconstruction images illustrating the structural difference among primary septa, secondary septa, and interseptal branches, viewed at the L-R plane. The locations of these slices are indicated by the corresponding lines shown in (A). (D) Skeleton and nodes on an isolated septum as shown in Fig. 2C. (E) A schematic diagram of the interseptal branches with N-3 (blue) and N-4 (red) nodes; (F) Histograms of different node types for interseptal branches originated from the two sides of the septum; (G) SEM image of a representative region of septum with manually detected interseptal branches colored by node types (blue ring: N-3 nodes; red ring: N-4 nodes; green ring: N-5 nodes); (H) A reconstruction image of a septum (PS-1, gray) overlaid by the positions of interseptal branches (ISB-1, red) from one side of the septum. White circles highlight the regions with the hole-like defects on the primary septum, which are “sealed” by connected interseptal branches. (I) A reconstruction image of a septum (PS-2, gray) overlaid by the adjacent interseptal branches on two sides of the septum (ISB-2, red, and ISB-3, blue). (For interpretation of the references to color in this figure legend, the reader is referred to the web version of this article.)

This is consistent with the previous quantitative analysis (Fig. 6C) where the ISB's are thinner and longer than the branches comprising the septum.

3.5. Structure of septum

Septum refers to the radially aligned stereom structure, which is the primary building block of *H. mamillatus*' spines in the edge region [15, 16]. As mentioned earlier, two types of septa are identified, i.e., the primary (PS) and secondary (SS) septa, where the insertion of secondary septa is ca. 1.25 mm away from the center, corresponding to sub-volume 7 in the analyzed volume (Fig. 1H and 2D, E).

In the region without the presence of secondary septa (e.g., sub-volume 4), each primary septum resembles a pseudo-hexagonal pattern when viewed in the L-R plane (Fig. S12). Each septum is directly connected to the adjacent primary septa via interseptal branches. In the sub-volumes with the presence of secondary septa (e.g., sub-volume 7–10), the positions of the primary septa, the secondary septa, and the interseptal branches can be clearly identified when viewed along the L direction based on X-ray projection images (Fig. 9A and B). The morphological characteristics of each structural type can be visualized by the cross-sectional reconstruction slices in the L-R plane (Fig. 9C). Again, the primary septa

(PS-1, -2, and -3) resemble the pseudo-hexagonal pattern consistently, yet the secondary septa (SS-2 and -3) have a more random pattern and less connectivity of branches than the primary septa (Fig. 9C). In addition, the interseptal branches (ISB-1, -2, -3, and -4) connecting a primary septum to an adjacent secondary septum typically exhibit circular cross sections, suggesting that these branches are primarily aligned along the C direction.

We then isolated an individual primary septum, as shown in the synchrotron X-ray projection image (Fig. 2C), and conducted a quantitative network analysis. The detected skeleton network again reveals the pseudo-hexagonal pattern of the septum structure in the background (Fig. 9D). Moreover, most of the node types are N-3 and N-4 nodes in the primary septa. Fig. 9E schematically illustrates the structures of N-3 (blue) and N-4 (red) nodes associated with the interseptal branches from a septum with an idealized hexagonal pattern. Statistical analysis on the detected node types indicates that the interseptal branches are extruded predominantly from N-3 (53%) and N-4 (36%) nodes of the septa and less from N-5 (9%) and N-6 (2%) nodes (Fig. 9F). SEM images of a primary septum with manually traced skeleton and positions of interseptal branches demonstrate consistent results with the 3D analysis (Fig. 9G). This structural design is also evident by directly overlaying the cross-sectional images of primary septa and its associated interseptal branches, where many interseptal branches are lo-

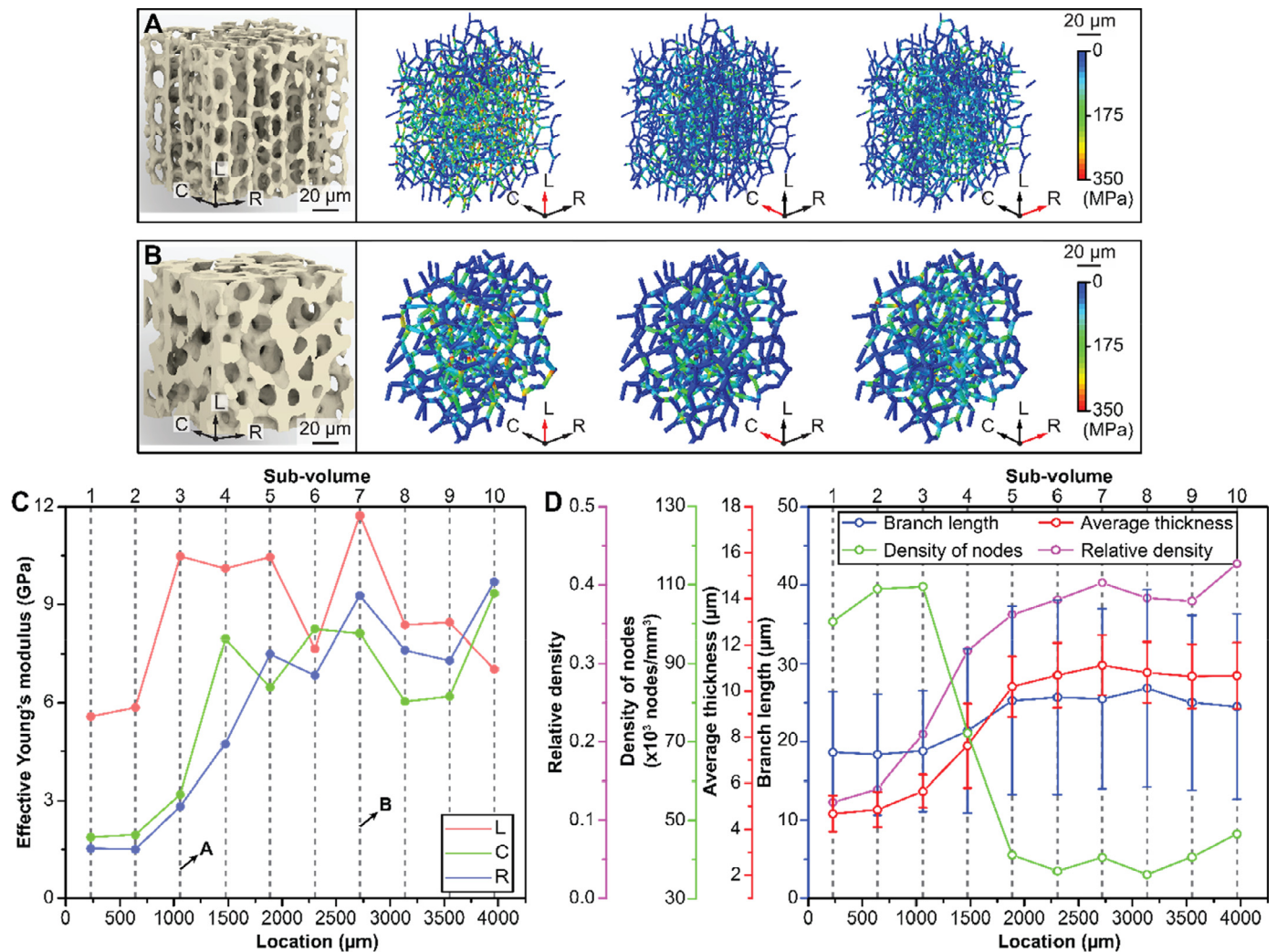


Fig. 10. Summary of the structural and mechanical variations across the volume of interest. Representative contours of von-Mises stress for sub-volume of portions (A) 3 and (B) 7. The red arrows in the coordinate system indicate the compression direction. (C) Variations of the effective Young's modulus in L, C, and R directions for the ten sub-volumes. (D) Variations of the branch length, average branch thickness, density of nodes, and the relative density for the ten sub-volumes. (For interpretation of the references to colour in this figure legend, the reader is referred to the web version of this article.)

cated on the branches instead of nodal points from septa (Fig. 9H). Moreover, the interseptal branches on two different sides of a septum are often dislocated from each other by extruding from different nodes of the septum, which results in the high fractions of N-3 and N-4 nodes for interseptal branches (Fig. 9I). Additionally, our quantitative analysis revealed that the interseptal branches are thinner (average thickness, $8.5 \pm 1.5 \mu\text{m}$ vs. $10.8 \pm 1.5 \mu\text{m}$), longer (branch length, $29.7 \pm 11.6 \mu\text{m}$ vs. $26.3 \pm 13.2 \mu\text{m}$), and slightly more curved on average (tortuosity, 1.21 ± 0.14 vs. 1.19 ± 0.15) than the branches comprising the septum.

3.6. Variation of mechanical properties

The variation of the cellular architecture from the center to the edge region revealed above suggests the local variation of mechanical properties in *H. mamillatus* spines, which is confirmed with our FE analysis on the extracted network skeleton (Fig. S13A). The von-Mises stress contours under compressions along the L, C, and R directions for two representative portions are shown in Fig. 10A and B (see Fig. S13B–D for complete results). The calculated effective Young's modulus of each sub-volume along the three principal directions are summarized in Fig. 10C. First of all, the effective modulus along the three principal directions in the sub-volume 1

and 2 (relative density, ~12 vol%) are always smaller than those in the other sub-volumes in the edge region (relative density, ~40 vol%) (Fig. 10C and D) [15]. Secondly, the effective modulus along the L direction is approximately three times higher than those along the R and C direction in the sub-volume 1–3 (on average, 7.3 GPa vs. 2.3 GPa vs. 2.0 GPa for L, R, C, respectively) (Fig. 10C). Furthermore, the effective modulus in three principal directions, especially the L direction, are dramatically increased since sub-volume 3. Compared with the center region, the edge region exhibits less mechanical anisotropy, but the effective modulus along the R and L direction is slightly higher than that in the C direction (Fig. 10C).

4. Discussions

4.1. Nodal configurations for lightweight and robust cellular design

In the first paper of this work series, we demonstrated that the stereom structure in the center region of *H. mamillatus* spines is constructed primarily with low-connectivity nodes (i.e., N-3 and N-4 nodes) [33]. The large volume analysis here reveals that this design rule also applies to the edge region, although the network organization pattern and the branch morphology vary sig-

nificantly from the spine center to edge. In particular, the majority of interseptal branches avoid connecting to the nodal points in the septum plane, maintaining a network structure consisting of low-connectivity nodes in septa. Construction of porous structures with low-connectivity nodes have been also observed in trabecular bone [42] and the stereom structure of the test of the sea urchin *Echinocyanus pusillus* [12].

It is well known that the nodal configuration directly affects the mechanical properties of cellular solids [41]. In particular, according to the node connectivity, cellular solids can be broadly classified into bending- and stretching-dominated structures, where the latter is usually more desired due to its high mechanical efficiency [41, 43]. For 3D foams, the minimum node connectivity to achieve stretching-dominated cellular structures is 12 [41]. This also represents one of the design strategies for developing stretching-dominated metamaterial lattices for improved mechanical performance recently [43–46]. Our analysis indicates that the stereom structure in sea urchin spines falls in the category of the bending-dominated lattice. It is currently unknown why these natural porous structures adopt this design rule, which may be constrained by the underlying formation processes. The relatively high density and rigid joints between branches may alleviate the bending deformation under external loads [39]. In addition, the N-3 and N-4 nodes in sea urchin spines approach ideal triangle-like and tetrahedron-like structural motifs, which are stable under tension and compression [41–44]. This also suggests that the branches connected by N-3 and N-4 nodes tend to evenly orient in 3D so that the least amount of material is used to maximally span the 3D space. A similar observation has been reported in human trabecular bone [41].

4.2. Galleried stereom in the center region and laminar stereom in the edge region

The combined results based on qualitative visualization and quantitative 3D network analysis suggests different stereom types in the center and edge region. In the center region, the stereom resembles more closely to the galleried type instead of the previously reported laminar type [14,15]. In this galleried structure, the stereom exhibits preferred branch alignment in the L direction, which is also evident from the branch chain analysis results [33]. These branches are further interconnected by horizontal branches, forming cylinder-like pores approximately parallel to the L direction [10]. This is supported by qualitative observations (Fig. 1G), branch orientations (Fig. 4C), and ring orientations (Fig. 8C). As discussed in [33], this structural organization correlates well with the stereom growth process in the center region, where the stereom initially grows as micro-spines oriented along the L direction, followed by the formation of horizontal “bridges” that connect adjacent micro-spines and finally the branch thickening via sequential mineral depositions [47].

In the edge region, the structural analysis on septa substantiates that the stereom in this region resembles the laminar type. Each lamina (*i.e.*, septum) is connected to adjacent ones by branches extruded towards the C direction (*i.e.*, interseptal branches) [10]. Each septum plane exhibits a pseudo-hexagonal porous pattern composed with thicker and shorter branches in comparison to the interseptal ones. These septum planes are radially aligned and connected with the “solid protrusions” of the growth rings. Moreover, secondary septa are inserted when the spacing between the primary septa is greater than ~50 μ m, resulting in the “pore-splitting” morphology reported earlier [15]. This strategy avoids the formation of very long branches, maintaining a relatively constant range of branch length throughout the cross section of the spine. As the building material of stereom is the brittle magnesium calcite

[48,49], this strategy may be beneficial to enhance the damage tolerance by eliminating minimizing the presence of long branches.

4.3. Structure-mechanics interplay for *H. mamillatus* spines

The different organization patterns and orientation-dependent branch thickness directly control the magnitudes and anisotropy of the stereom’s local mechanical properties. First, although the center region has a significantly higher node density, the thin branches result in the high porosity and hence the lower effective modulus in all directions in comparison to the edge region. In addition, the galleried stereom in the center region with thicker branches aligned towards the L direction leads to a high mechanical anisotropy, *i.e.*, higher stiffness in the L direction. In the edge region, as the primary septa planes are radially aligned (*i.e.*, the L-R plane) and consist of thicker and shorter branches in comparison to interseptal branches, the stereom exhibits higher stiffness in the R and L directions. Compared to the center region, the stereom in the edge region is more isotropic due to the presence of interseptal branches aligned towards the C direction.

Sea urchin spines are subject to different types of external forces, including hydrodynamic forces from ocean waves, attacks from predators, and forces to wedge themselves into small holes for protection [11,25,50,51]. In particular, some sea urchins “sacrifice” their spines to pierce to their predators and break off [25]. Therefore, the loading modes for sea urchin spines are complex, which may include axial compression, axial torsion and bending [11,25,50]. The *H. mamillatus* spines achieve a high axial stiffness (*i.e.*, in the L direction) as evident by the fact that the local effective stiffness in both center and edge regions are the highest compared to the other two directions. This is due to the longitudinal alignment of thicker branches in the center region and the septa structure in the L-R plane. In addition, the bending and torsional resistance are enhanced through the gradual increase in local stiffness in three principal directions due to the increase in branch thickness and relative density from the spine center to edge. This follows the general strategy to increase the moment of inertia by placing more materials at the periphery, a classical strategy utilized by a variety of natural systems to enhance bending and torsional resistance while minimizing weight [16,52,53]. Lastly, the radial alignment of “dense” septum structures also enhances the resistance to radial compression (*i.e.*, high relative modulus in the R direction). A similar design strategy has been observed in the mineralized tiles (known as tesserae) in the skeletons of elasmobranch fishes, where the stiffness of individual tessera in the radial direction is enhanced through the radially-aligned “spoke-like” structures with a high mineral density and local mechanical properties [54].

4.4. Local structural modifications

Structural defects have been shown to play a critical role in controlling the mechanical performance of cellular solids or lattice structures [55–59]. Our network analysis reveals that, although the stereom structure follows some general organization patterns, such as the galleried and laminar forms in the center and edge region respectively, local structural modifications exist, particularly in the regions that appear to be structural defects. For example, a careful examination of the pseudo-hexagonal pattern of the primary septa reveals the presence of large holes (*ca.* 30 μ m in comparison to the typical hole size of *ca.* 20 μ m for septa) (yellow arrows in PS-1 and PS-3, Fig. 9C). The interseptal branches “close” these large defect-like holes by forming interconnected branches as shown in the overlaid image between PS and ISB (white circles, Fig. 9H). In addition, we observed that horizontal branches bridge large transverse holes in the center region, which may serve as

reinforcing structures to the local defects [33]. These observations indicate that, unlike engineering lattice structures, organisms are able to modify and reinforce local defects in their porous structures with additional branches and connections.

4.5. Limitations of current work

Several aspects require further investigations in order to fully understand the mechanical designs of sea urchin spines. First of all, the growth ring has been shown to play an important role in determining the mechanical performance of *H. mamillatus* spine, especially the inelastic behavior [16,60]. Further study by combining dense growth rings and the gradient stereom analyzed here could offer further insights. Secondly, although our beam model-based FE analysis by using the extracted cellular network provides an efficient approach to evaluate local mechanical variations, it cannot capture the contributions from the curved branch and nodal morphology in stereom. Unlike stereom structures, many conventional and architected engineering cellular materials comprise of branches with uniform thickness and sharp connections [44–46,61]. Further analysis can be achieved by incorporating the obtained branch profiling information with geometric modeling methods such as implicit functions and BLINN transformation [62,63]. In addition, our current modeling approach allows us to construct arbitrary models with given network topology and hence isolate the effect of different parameters (e.g., network topology, distribution of branch thickness or aspect ratio, etc.). The anisotropic mechanical properties of calcite should be also considered in further analysis of the overall mechanical performance of sea urchin spines, as they are often considered as large single crystals [64].

5. Conclusion

In this study, we adopted a multiscale network analysis algorithm developed in the first paper to conduct, to the best of our knowledge, the first comprehensive, quantitative analysis of the cellular network on the *H. mamillatus* spines over a large volume in 3D [33]. The structural descriptors, including node characteristics, branch thickness, length, distance, tortuosity, orientation, and ring structures, were used to investigate the structural variation from the spine center to the edge region over millimeter scales. At the individual branch and node level, our analysis shows that the porous stereom network in the spine is primarily composed of nearly ideal N-3 and N-4 nodes, allowing for the maximal occupation of 3D space using the least amount of materials and mechanically robust design. From the center to the edge region close to the first growth ring, despite of the decreased number density of branches, the branch length increases ~50% yet the branch thickness doubles, collaboratively resulting in a gradual increase of relative density of the stereom from ca. 12% in the center region to ca. 40% in the edge region. In addition, the branches exhibit location- and orientation-dependent branch morphology variations from the center to the edge based on the fitting results of the branch profile.

Our analysis also reveals the drastic difference in the 3D network organization patterns between the center and the edge region. The center region is composed of branches oriented parallel or perpendicular to the L direction, exhibiting a galleried stereom type instead of the laminar stereom type as reported earlier. In the edge region, the stereom exhibits a laminar construction based on “septa” that are aligned along the R direction. Each primary septum resembles a pseudo-hexagonal pattern on the L-R plane, which has branch thickness, on average, ~1 μm thicker than the interseptal branches connecting to the adjacent septa. Moreover, approximately 50% of the interseptal branches are connected to the branches instead of nodal points of the septum wall, forming

many N-3 nodes. As the spacing between the primary septa increases towards the spine's edge, initially less-ordered secondary septa with thinner branches are inserted between adjacent primary septa. With the quantified branch- and network-level information, the local mechanical properties of the stereom structure are investigated, which reveals the underlying functionally graded design, particularly in terms of effective modulus variation and mechanical anisotropy.

The quantitative multiscale cellular network analysis results conducted on the *H. mamillatus* spines here could provide important insights in the design and development of the 3D bio-inspired materials and structures with low density, high strength, and damage tolerance. Also, enabled by the extensive progress of advanced 3D additive manufacturing, the fabrication of these functionally-graded, micro- or nano-architected structures inspired by sea urchin spines may become feasible [44–46,61,65]. We also envision that this large-scale cellular network analysis approach could be readily applied to other sea urchin spines for potential inter-specific structural comparison, or other echinoderms' porous skeletal elements such as sea star's ossicles, or other natural cellular materials in general.

Declaration of Competing Interest

The authors declare that they have no known competing financial interests or personal relationships that could have appeared to influence the work reported in this paper.

CRediT authorship contribution statement

Hongshun Chen: Conceptualization, Formal analysis, Investigation, Methodology, Writing - original draft. **Ting Yang:** Investigation, Formal analysis, Methodology, Writing - original draft. **Ziling Wu:** Methodology, Writing - review & editing. **Zhifei Deng:** Writing - review & editing. **Yunhui Zhu:** Conceptualization, Investigation, Writing - review & editing. **Ling Li:** Investigation, Writing - review & editing, Conceptualization, Supervision.

Acknowledgments

We gratefully acknowledge the National Science Foundation under award number CMMI-1825646 and the Air Force Office of Scientific Research under award number FA9550-19-1-0033. Use of the Advanced Photon Source, an Office of Science User Facility operated for the U.S. Department of Energy (DOE) Office of Science by Argonne National Laboratory, was supported by the U.S. DOE under Contract No. DE-AC02-06CH11357. The authors greatly acknowledge the technical support from the beamline scientists Dr. Francesco De Carlo and Pavel D. Shevchenko at APS.

Supplementary materials

Supplementary material associated with this article can be found, in the online version, at doi:[10.1016/j.actbio.2020.03.006](https://doi.org/10.1016/j.actbio.2020.03.006).

References

- [1] E.I.S. Flores, M.I. Friswell, Multi-scale finite element model for a new material inspired by the mechanics and structure of wood cell-walls, *J. Mech. Phys. Solids* 60 (7) (2012) 1296–1309.
- [2] L.J. Gibson, The hierarchical structure and mechanics of plant materials, *J. R. Soc. Interface* 9 (76) (2012) 2749–2766.
- [3] M. Borrega, L.J. Gibson, Mechanics of balsa (*Ochroma pyramidale*) wood, *Mech. Mater* 84 (2015) 75–90.
- [4] R.K. Nalla, J.H. Kinney, R.O. Ritchie, Mechanistic fracture criteria for the failure of human cortical bone, *Nat. Mater.* 2 (3) (2003) 164–168.
- [5] R.O. Ritchie, J.H. Kinney, J.J. Kruzic, R.K. Nalla, A fracture mechanics and mechanistic approach to the failure of cortical bone, *Fatigue Fract. Eng. M.* 28 (4) (2005) 345–371.

- [6] T.M. Keaveny, E.F. Morgan, G.L. Niebur, O.C. Yeh, Biomechanics of trabecular bone, *Annu. Rev. Biomed. Eng.* 3 (2001) 307–333.
- [7] J.H. Nebelsick, J.F. Dynowski, J.N. Grossmann, C. Totzke, Echinoderms: hierarchically organized light weight skeletons, in: C. Hamm (Ed.), *Biologically Inspired Systems*, Springer, Dordrecht, 2015, pp. 141–155.
- [8] M. Telford, Echinoderm spine structure, feeding and host relationships of four species of *dissodactylus* (Brachyura: pinnotheridae), *Bull. Mar. Sci.* 32 (2) (1982) 584–594.
- [9] J. Weber, R. Greer, B. Voight, E. White, R. Roy, Unusual strength properties of echinoderm calcite related to structure, *J. Ultrastruct. Res.* 26 (5–6) (1969) 355–366.
- [10] A.B. Smith, Stereom microstructure of the echinoid test, *Spec. Pap. Palaeontol.* 25 (1980) 1–81.
- [11] V. Presser, S. Schultheiß, C. Berthold, K. Nickel, Sea urchin spines as a model-system for permeable, light-weight ceramics with graceful failure behavior. Part I. Mechanical behavior of sea urchin spines under compression, *J. Bionic Eng.* 6 (3) (2009) 203–213.
- [12] T.B. Grun, J.H. Nebelsick, Structural design of the echinoid's trabecular system, *PLoS ONE* 13 (9) (2018).
- [13] N. Grossmann, J.H. Nebelsick, Stereom differentiation in spines of *plococidaris verticillata*, *heterocentrotus mammillatus* and other regular sea urchins, in: C. Johnson (Ed.), *Proceedings of the 13th International Echinoderm Conference*, University of Tasmania, Hobart Tasmania, Australia, 2013, pp. 97–104.
- [14] J.N. Grossmann, J.H. Nebelsick, Comparative morphological and structural analysis of selected cidaroid and camarodont sea urchin spines, *Zoomorphology* 132 (3) (2013) 301–315.
- [15] C. Lauer, T.B. Grun, I. Zutterkirch, R. Jemmali, J.H. Nebelsick, K.G. Nickel, Morphology and porosity of the spines of the sea urchin *heterocentrotus mammillatus* and their implications on the mechanical performance, *Zoomorphology* 137 (1) (2018) 139–154.
- [16] C. Lauer, K. Sillmann, S. Haußmann, K.G. Nickel, Strength, elasticity and the limits of energy dissipation in two related sea urchin spines with biomimetic potential, *Bioinspir. Biomim.* 14 (1) (2018) 016018.
- [17] K.G. Nickel, K. Klang, C. Lauer, G. Buck, Sea urchin spines as role models for biologic design and integrative structures, in: S. Heuss-Aßbichler, G. Amthauer, M. John (Eds.), *Highlights of Applied Mineralogy*, De Gruyter, Berlin, Germany, 2018, pp. 273–287.
- [18] M. Jensen, The ultrastructure of the echinoid skeleton, *Sarsia* 48 (1) (1972) 39–48.
- [19] V. Presser, S. Schultheiss, C. Kohler, C. Berthold, K.G. Nickel, A. Vohrer, H. Finckh, T. Stegmaier, Lessons from nature for the construction of ceramic cellular materials for superior energy absorption, *Adv. Eng. Mater.* 13 (11) (2011) 1042–1049.
- [20] S. Schmier, C. Lauer, I. Schafer, K. Klang, G. Bauer, M. Thielen, K. Termin, C. Berthold, S. Schmauder, T. Speck, K.G. Nickel, Developing the experimental basis for an evaluation of scaling properties of brittle and 'Quasi-Brittle' biological materials, in: J. Knippers, K. Nickel, T. Speck (Eds.), *Biomimetic Research for Architecture and Building Construction: Biological Design and Integrative Structures*, Springer International Publishing, Switzerland, 2016, pp. 277–294.
- [21] N. Toader, W. Sobek, K.G. Nickel, Energy absorption in functionally graded concrete bioinspired by sea urchin spines, *J. Bionic Eng.* 14 (2) (2017) 369–378.
- [22] M.D.C. Carnevali, F. Bonasoro, G. Melone, Microstructure and mechanical design in the lantern ossicles of the regular sea-urchin *paracentrotus lividus* a scanning electron microscope study, *Ital. J. Zool.* 58 (1) (1991) 1–42.
- [23] J.N. Grossmann, Stereom Differentiation in Sea Urchin Spines Under Special Consideration As a Model For a New Impact Protective System, University of Tübingen, 2010.
- [24] S. Stock, K. Ignatiev, F. De Carlo, Very high resolution synchrotron microCT of sea urchin ossicle structure, in: T. Heinzeller, J.H. Nebelsick (Eds.), *Proceedings of the 11th International Echinoderm Conference*, CRC Press, Munich, 2004, pp. 353–358.
- [25] N. Tsafnat, J.D.F. Gerald, H.N. Le, Z.H. Stachurski, Micromechanics of sea urchin spines, *PLoS ONE* 7 (9) (2012) e44140.
- [26] V. Presser, K. Gerlach, A. Vohrer, K.G. Nickel, W.F. Dreher, Determination of the elastic modulus of highly porous samples by nanoindentation: a case study on sea urchin spines, *J. Mater. Sci.* 45 (9) (2010) 2408–2418.
- [27] T.B. Grun, J.H. Nebelsick, Structural design of the minute clypeasteroid echinoid *echinocyamus pusillus*, *R. Soc. Open Sci.* 5 (5) (2018) 171323.
- [28] J. Schindelin, I. Arganda-Carreras, E. Frise, V. Kaynig, M. Longair, T. Pietzsch, S. Preibisch, C. Rueden, S. Saalfeld, B. Schmid, J.Y. Tinevez, D.J. White, V. Hartenstein, K. Eliceiri, P. Tomancak, A. Cardona, Fiji: an open-source platform for biological-image analysis, *Nat. Methods* 9 (7) (2012) 676–682.
- [29] D. Guersoy, F. De Carlo, X.H. Xiao, C. Jacobsen, TomoPy: a framework for the analysis of synchrotron tomographic data, *J. Synchrotron Radiat.* 21 (2014) 1188–1193.
- [30] B.A. Dowd, G.H. Campbell, R.B. Marr, V. Nagarkar, S. Tipnis, L. Axe, D.P. Sidons, Developments in synchrotron x-ray computed microtomography at the national synchrotron light source, *P. Soc. Photo Opt. Ins.* 3772 (1999) 224–236.
- [31] C. Sommer, C. Straehle, U. Kothe, F.A. Hamprecht, Ilastik: interactive learning and segmentation toolkit, in: *Proceedings of the 8th IEEE International Symposium on Biomedical Imaging: From Nano to Macro*, Chicago, IL, USA, 2011, pp. 230–233.
- [32] L. Breiman, Random forests, *Mach. Learn.* 45 (1) (2001) 5–32.
- [33] T. Yang, Z. Wu, H. Chen, Y. Zhu, L. Li, Quantitative 3D structural analysis of the cellular microstructures of sea urchin spines (I): methodology, *Acta Biomater.* doi:10.1016/j.actbio.2020.02.034.
- [34] W.Y. Jang, A.M. Kraynik, S. Kyriakides, On the microstructure of open-cell foams and its effect on elastic properties, *Int. J. Solids Struct.* 45 (7–8) (2008) 1845–1875.
- [35] A. Liebscher, C. Redenbach, Statistical analysis of the local strut thickness of open cell foams, *Image Anal. Stereol.* 32 (1) (2013) 1–12.
- [36] P. De Jaeger, C. T'Joens, H. Huisseune, B. Arneel, M. De Paepe, An experimentally validated and parameterized periodic unit-cell reconstruction of open-cell foams, *J. Appl. Phys.* 109 (10) (2011) 103519.
- [37] D. Dassault Systèmes, Abaqus Analysis User's guide, Technical Report Abaqus 6.16 Documentation, Simulia Corp., 2016.
- [38] L.F. Zhu, M. Friak, L. Lympirakis, H. Titrian, U. Aydin, A.M. Janus, H.O. Fabritius, A. Ziegler, S. Nikolov, P. Hemzalova, D. Raabe, J. Neugebauer, Ab initio study of single-crystalline and polycrystalline elastic properties of Mg-substituted calcite crystals, *J. Mech. Behav. Biomed. Mater.* 20 (2013) 296–304.
- [39] L.R. Meza, G.P. Phlipot, C.M. Portela, A. Maggi, L.C. Montemayor, A. Comella, D.M. Kochmann, J.R. Greer, Reexamining the mechanical property space of three-dimensional lattice architectures, *Acta Mater* 140 (2017) 424–432.
- [40] T.A. Ebert, The non-periodic nature of growth rings in echinoid spines, in: B.F. Keegan, B.D. O'Connor (Eds.), *Proceedings of the International Echinoderm Conference*, Rotterdam: A.A. Balkema, Galway, 1984, pp. 261–267.
- [41] V.S. Deshpande, M.F. Ashby, N.A. Fleck, Foam topology: bending versus stretching dominated architectures, *Acta Mater.* 49 (6) (2001) 1035–1040.
- [42] N. Reznikov, H. Chase, Y.B. Zvi, V. Tarle, M. Singer, V. Brumfeld, R. Shahar, S. Weiner, Inter-trabecular angle: a parameter of trabecular bone architecture in the human proximal femur that reveals underlying topological motifs, *Acta Biomater.* 44 (2016) 65–72.
- [43] L.J. Gibson, M.F. Ashby, *Cellular Solids: Structure and Properties*, 2nd ed., Cambridge University Press, Cambridge, 1997.
- [44] X.Y. Zheng, W. Smith, J. Jackson, B. Moran, H.C. Cui, D. Chen, J.C. Ye, N. Fang, N. Rodriguez, T. Weisgraber, C.M. Spadaccini, Multiscale metallic metamaterials, *Nat. Mater.* 15 (10) (2016) 1100–1106.
- [45] X. Zheng, H. Lee, T.H. Weisgraber, M. Shusteff, J. DeOtte, E.B. Duoss, J.D. Kuntz, M.M. Biener, Q. Ge, J.A. Jackson, Ultralight, ultrastiff mechanical metamaterials, *Science* 344 (6190) (2014) 1373–1377.
- [46] L.R. Meza, S. Das, J.R. Greer, Strong, lightweight, and recoverable three-dimensional ceramic nanolattices, *Science* 345 (6202) (2014) 1322–1326.
- [47] P. Gorzelak, J. Stolarski, P. Dubois, C. Kopp, A. Meibom, (26)mg labeling of the sea urchin regenerating spine: insights into echinoderm biomineralization process, *J. Struct. Biol.* 176 (1) (2011) 119–126.
- [48] J.N. Weber, The incorporation of magnesium into the skeletal calcites of echinoderms, *Am. J. Sci.* 267 (5) (1969) 537–566.
- [49] J. Seto, Y.R. Ma, S.A. Davis, F. Meldrum, A. Gourrier, Y.Y. Kim, U. Schilde, M. Sztucki, M. Burghammer, S. Maltsev, C. Jager, H. Colfen, Structure-property relationships of a biological mesocrystal in the adult sea urchin spine, *Proc. Natl. Acad. Sci. U.S.A.* 109 (10) (2012) 3699–3704.
- [50] T. Chen, *Microstructure and Micromechanics of the Sea Urchin, Colobocentrotus Atratus*, Massachusetts Institute of Technology, 2011.
- [51] R.R. Strathmann, The role of spines in preventing structural damage to echinoid tests, *Paleobiology* 7 (3) (1981) 400–406.
- [52] L.J. Gibson, Biomechanics of cellular solids, *J. Biomech.* 38 (3) (2005) 377–399.
- [53] M.A. Dawson, L.J. Gibson, Optimization of cylindrical shells with compliant cores, *Int. J. Solids Struct.* 44 (3–4) (2007) 1145–1160.
- [54] R. Seidel, A. Roschger, L. Li, J.J. Bizzarro, Q.T. Zhang, J. Yin, T. Yang, J.C. Weaver, P. Fratzl, P. Roschger, M.N. Dean, Mechanical properties of stingray tesserae: high-resolution correlative analysis of mineral density and indentation moduli in tessellated cartilage, *Acta Biomater.* 96 (2019) 421–435.
- [55] I. Quintana-Alonso, N.A. Fleck, Fracture of Brittle Lattice Materials: A Review, *Major Accomplishments in Composite Materials and Sandwich Structures: An Anthology ONR Sponsored Research*, (2009) 799–816.
- [56] N.A. Fleck, X.M. Qiu, The damage tolerance of elastic-brittle, two-dimensional isotropic lattices, *J. Mech. Phys. Solids* 55 (3) (2007) 562–588.
- [57] N.E.R. Romijn, N.A. Fleck, The fracture toughness of planar lattices: imperfection sensitivity, *J. Mech. Phys. Solids* 55 (12) (2007) 2538–2564.
- [58] L.C. Montemayor, W.H. Wong, Y.W. Zhang, J.R. Greer, Insensitivity to flaws leads to damage tolerance in brittle architected meta-materials, *Sci. Rep.* 6 (2016) 20570.
- [59] M.S. Pham, C. Liu, I. Todd, J. Lertthanasarn, Damage-tolerant architected materials inspired by crystal microstructure, *Nature* 565 (7739) (2019) 305–311.
- [60] C. Lauer, S. Schmier, T. Speck, K.G. Nickel, Strength-size relationships in two porous biological materials, *Acta Biomater.* 77 (2018) 322–332.
- [61] L.R. Meza, A.J. Zelhofer, N. Clarke, A.J. Mateos, D.M. Kochmann, J.R. Greer, Resilient 3D hierarchical architected metamaterials, *Proc. Natl. Acad. Sci. U.S.A.* 112 (37) (2015) 11502–11507.
- [62] J.F. Blinn, A generalization of algebraic surface drawing, *ACM Trans. Graph.* 1 (3) (1982) 235–256.
- [63] J. Storm, M. Abendroth, M. Emmel, T. Liedke, U. Ballaschk, C. Voigt, T. Sieber, M. Kuna, Geometrical modelling of foam structures using implicit functions, *Int. J. Solids Struct.* 50 (3–4) (2013) 548–555.
- [64] X. Su, S. Kamat, A.H. Heuer, The structure of sea urchin spines, large biogenic single crystals of calcite, *J. Mater. Sci.* 35 (22) (2000) 5545–5551.
- [65] R. Lontas, J.R. Greer, 3D nano-architected metallic glass: size effect suppresses catastrophic failure, *Acta Mater.* 133 (2017) 393–407.